



T. Kaiser · A. Menzel

A finite deformation electro-mechanically coupled computational multiscale formulation for electrical conductors

Received: 9 November 2020 / Revised: 22 March 2021 / Accepted: 8 April 2021 / Published online: 5 August 2021
© The Author(s) 2021

Abstract Motivated by the influence of deformation-induced microcracks on the effective electrical properties at the macroscale, an electro-mechanically coupled computational multiscale formulation for electrical conductors is proposed. The formulation accounts for finite deformation processes and is a direct extension of the fundamental theoretical developments presented by Kaiser and Menzel (Arch Appl Mech 91:1509–1526, 2021) who assume a geometrically linearised setting. More specifically speaking, averaging theorems for the electric field quantities are proposed and boundary conditions that a priori fulfil the extended Hill–Mandel condition of the electro-mechanically coupled problem are discussed. A study of representative boundary value problems in two- and three-dimensional settings eventually shows the applicability of the proposed formulation and reveals the severe influence of microscale deformation processes on the effective electrical properties at the macroscale.

1 Introduction

Computational multiscale formulations are well-established numerical tools to predict macroscopic material properties from the underlying heterogeneous microstructure. To this end, detailed information on the microstructure is collected in so-called representative volume elements, [11, 36], and classic constitutive equations are substituted by detailed microstructure simulations. By using averaging theorems, macroscopic field quantities are related to their microscopic analogues, and the effective material response at the macroscale is predicted. Detailed information on micromechanical processes is thus taken into account in multiscale simulations which are, for instance, used in the development process of advanced materials with tailored properties or functionalities, [6]. Vice versa, multiscale methods contribute to an understanding of experimentally recorded data at the macroscale by relating the properties of single phases and interfaces at the microscale to the effective macroscale material response.

In this regard, an electro-mechanically coupled computational multiscale formulation for electrical conductors is proposed in the present contribution that allows to study the influence of microscale deformation processes on the effective electrical properties at the macroscale. In particular, this contribution is motivated by experimental findings on material thin films [7]. In these experiments, copper thin films are cyclically strained, and the effective electrical resistance as a function of deformation is measured. The recorded increase in electrical resistance with increasing deformation is explained by the formation of mechanically induced

T. Kaiser (✉) · A. Menzel
Institute of Mechanics, TU Dortmund University, Leonhard-Euler-Str. 5, 44227 Dortmund, Germany
E-mail: tobias.kaiser@tu-dortmund.de

A. Menzel
Division of Solid Mechanics, Lund University, P.O. Box 118, 22100 Lund, Sweden
E-mail: andreas.menzel@solid.lth.se
E-mail: andreas.menzel@udo.edu

microcracks. Metal thin films are the basis for flexible electronic devices such as wearable sensors [10,31] and foldable displays [5,22], and a detailed understanding of failure mechanisms and of deformation-induced changes of the effective electrical properties is required to ensure their functionality. Furthermore, the proposed multiscale formulation is expected to contribute to the development process of advanced non-destructive electrical resistance-based testing methods used to analyse defect structures in specimens, e.g. [23].

The computational multiscale formulation for electro-mechanically coupled problems proposed in the present contribution relies on and is a direct extension of well-established computational homogenisation schemes as presented in the review paper [13]. For purely mechanical problems, first-order computational homogenisation schemes are, for instance, discussed in [12,14,24,27–30]. The extension to generalised continuum theories by additionally taking the second gradient of the placement field into account has been studied in e.g. [17,25,26,32]. Moreover, computational homogenisation schemes for thermo-mechanically coupled problems are addressed in [2,3,33,37,39], formulations for magneto-mechanically coupled problems are discussed in [18,38], and formulations that focus on the simulation of piezo- and ferroelectric materials are elaborated in [20,21,35]. Compared to the present formulation, the latter developments on electro-active solids are based on the fundamentals of electrostatics, whereas the present formulation relies (amongst others) on the continuity equation for the electric current. Moreover, the flow of electric charge is intrinsically dissipative and stipulates an inequality comparable to Fourier's inequality of thermal problems that restricts the particular form of the constitutive equation for the electric current density vector. This is in striking contrast to the (possibly) reversible processes of electro-active solids studied in [20,21,35]. From a materials science point of view, piezo- and dielectric moduli are in the focus of the latter works, whereas the electrical conductivity tensor is the primary material parameter that characterises the process studied in the present contribution. More specifically speaking, the present contribution is a direct extension of the fundamental developments on multiscale formulations for electrical conductors discussed in [19], subject to the assumption of linearised kinematics, to a finite deformation setting. This extension is essential to capture the effect of (inhomogeneous) geometry changes at the microscale on the effective macroscale conductivity tensor.

For the convenience of the reader, the article is organised similar to its small strain analogue [19]: Based on Maxwell's equations of electromagnetism, the governing set of partial differential equations of the electro-mechanically coupled continuum under consideration is briefly summarised in Sect. 2. These fundamentals serve as the basis for the multiscale formulation proposed in Sect. 3. A finite element-based implementation is then discussed in Sect. 4 before representative boundary value problems in two- and three dimensional settings are studied in Sect. 5. The findings are summarised and concluding remarks are drawn in Sect. 6.

1.1 Notation

Let $\alpha, \beta, \gamma, \delta$ denote tensor-valued quantities of first order, and let \otimes denote the standard dyadic product. With these definitions at hand, the single tensor contraction will be used in the sense $[\alpha \otimes \beta] \cdot [\gamma \otimes \delta] = [\beta \cdot \gamma][\alpha \otimes \delta]$ and the double tensor contraction in the sense $[\alpha \otimes \beta] : [\gamma \otimes \delta] = [\alpha \cdot \gamma][\beta \cdot \delta]$. In addition to the standard dyadic product, the generalised dyadic products $[\alpha \otimes \beta] \overline{\otimes} [\gamma \otimes \delta] = [\alpha \otimes \gamma] \otimes [\beta \otimes \delta]$ and $[\alpha \otimes \beta] \underline{\otimes} [\gamma \otimes \delta] = [\alpha \otimes \gamma] \otimes [\delta \otimes \beta]$ are introduced to allow for a compact notation. Moreover, gradient, divergence, and curl operators with respect to referential and spatial coordinates are denoted as $\nabla_{\mathbf{X}}, \nabla_{\mathbf{X}} \cdot, \nabla_{\mathbf{X}} \times$, respectively, $\nabla_{\mathbf{x}}, \nabla_{\mathbf{x}} \cdot, \nabla_{\mathbf{x}} \times$, the material time derivative as $\dot{\bullet}$, and the second-order identity tensor as \mathbf{I} .

2 Continuum thermodynamics

The thermodynamic fundamentals of (thermo-magneto-)electro-mechanically coupled problems in a finite deformation setting will briefly be summarised in this Section. In particular, Sect. 2.1 focuses on kinematics and on the mechanical subproblem, Sect. 2.2 focuses on the electrical subproblem, and Sect. 2.3 focuses on the conservation of energy and on the dissipation inequality. A more detailed elaboration of the governing set of field equations is presented in e.g. [16].

2.1 Kinematics and mechanical subproblem

Let particles be identified by their position vectors $\mathbf{X} \in \mathcal{B}_0$ at time $t_0 \in \mathbb{R}$, and let the region in space that is occupied by the body under consideration at time t_0 be denoted by $\mathcal{B}_0 \subset \mathbb{R}^3$. Moreover, let $\mathbf{x} \in \mathcal{B}_t$ denote the

position vector of a particle at time $t \geq t_0$ and let $\mathcal{B}_t \subset \mathbb{R}^3$ denote the spatial configuration of the body. The deformation map relating the referential and the current configuration is given by $\boldsymbol{\varphi}(\mathbf{X}, t) : \mathcal{B}_0 \times \mathbb{R} \rightarrow \mathcal{B}_t \subset \mathbb{R}^3$. The associated map acting on the tangent space is $\mathbf{F} = \partial\boldsymbol{\varphi}/\partial\mathbf{X}$, with cofactor $\text{cof}(\mathbf{F}) = J_{\mathbf{F}}\mathbf{F}^{-t}$ and with Jacobian $J_{\mathbf{F}} = \det(\mathbf{F}) > 0$. Making use of the latter definitions and denoting referential and spatial outward unit normal vectors by \mathbf{N} , respectively \mathbf{n} , transformation rules for (referential and spatial) volume, surface and line elements follow accordingly: $J_{\mathbf{F}} dV = dv$, $\text{cof}(\mathbf{F}) \cdot \mathbf{N} da = \mathbf{n} da$, $\mathbf{F} \cdot d\mathbf{S} = ds$.

The mechanical subproblem is governed by the balance equation of linear momentum in its classic, referential form

$$\nabla_{\mathbf{X}} \cdot \mathbf{P} + \rho_0 \mathbf{f} = \rho_0 \ddot{\mathbf{x}}, \quad (1)$$

with the Piola stress tensor \mathbf{P} , the (mass-specific) body force vector \mathbf{f} and the mass density with respect to the reference configuration ρ_0 . The balance equation of angular momentum reduces to the symmetry condition of the Cauchy stress tensor $\boldsymbol{\sigma} = \boldsymbol{\sigma}^t$ with $\mathbf{P} = J_{\mathbf{F}} \boldsymbol{\sigma} \cdot \mathbf{F}^{-t}$, and is accounted for by the specific choice of the constitutive equations. According to Cauchy's theorem, linear relations between the stress tensors, the outward unit normal vectors, and the traction vectors \mathbf{t}_t , respectively, \mathbf{t}_0 , are assumed

$$\mathbf{t}_t = \boldsymbol{\sigma} \cdot \mathbf{n}, \quad (2.1)$$

$$\mathbf{t}_0 = \mathbf{P} \cdot \mathbf{N}. \quad (2.2)$$

2.2 Electrical subproblem

Maxwell's equations form the foundation for the simulation of general electro-magnetic problems. With respect to the spatial configuration, these are given by

$$\text{Gauss's electric law (spatial)} \quad \int_{\partial\mathcal{B}_t} \mathbf{d} \cdot \mathbf{n} da = \int_{\mathcal{B}_t} \rho_{ft} dv \quad (3.1)$$

$$\text{Gauss's magnetic law (spatial)} \quad \int_{\partial\mathcal{B}_t} \mathbf{b} \cdot \mathbf{n} da = 0 \quad (3.2)$$

$$\text{Faraday's law of induction (spatial)} \quad \int_{\partial\mathcal{A}_t} \boldsymbol{\epsilon} \cdot d\mathbf{s} = - \frac{d}{dt} \int_{\mathcal{A}_t} \mathbf{b} \cdot \mathbf{n} da \quad (3.3)$$

$$\text{Ampère's circuital law (spatial)} \quad \int_{\partial\mathcal{A}_t} \boldsymbol{\eta} \cdot d\mathbf{s} = \int_{\mathcal{A}_t} \mathbf{j} \cdot \mathbf{n} da + \frac{d}{dt} \int_{\mathcal{A}_t} \mathbf{d} \cdot \mathbf{n} da \quad (3.4)$$

where \mathcal{A}_t denotes a surface that, in general, needs not to be closed. Moreover, the set of equations (3) includes the continuity equation for the electric current which follows immediately from the evaluation of (3.4) for the special case of a closed surface and from the insertion of (3.1) in the ensuing equation

$$0 = \int_{\partial\mathcal{B}_t} \mathbf{j} \cdot \mathbf{n} da + \frac{d}{dt} \int_{\mathcal{B}_t} \rho_{ft} dv. \quad (4)$$

It is remarked that the set of balance equations (3) is formulated in terms of the effective electric field vector $\boldsymbol{\epsilon}$ (also referred to as the electromotive intensity) and the effective magnetic field vector $\boldsymbol{\eta}$ (also referred to as the magnetomotive intensity). The balance equations can equivalently be formulated in terms of the Minkowskian electric field vector \mathbf{e} and the Minkowskian magnetic field vector \mathbf{h} defined as

$$\mathbf{e} = \boldsymbol{\epsilon} - \dot{\mathbf{x}} \times \mathbf{b}, \quad (5.1)$$

$$\mathbf{h} = \boldsymbol{\eta} + \dot{\mathbf{x}} \times \mathbf{d}. \quad (5.2)$$

The spatial representations of the (conductive) electric current density vector \mathbf{j} , of the dielectric displacement vector \mathbf{d} , and of the electric field vector $\boldsymbol{\epsilon}$, are related to their referential counterparts via

$$\mathbf{J} = J_{\mathbf{F}} \mathbf{F}^{-1} \cdot \mathbf{j}, \quad (6.1)$$

$$\mathbf{D} = J_{\mathbf{F}} \mathbf{F}^{-1} \cdot \mathbf{d}, \quad (6.2)$$

$$\boldsymbol{\mathcal{E}} = \mathbf{F}^t \cdot \boldsymbol{\epsilon}. \quad (6.3)$$

Moreover, the magnetic flux density \mathbf{b} , the magnetic field vector \mathbf{h} , and the (volume specific) free charge density ρ_{ft} transform according to

$$\mathbf{B} = J_{\mathbf{F}} \mathbf{F}^{-1} \cdot \mathbf{b}, \quad (7.1)$$

$$\mathcal{H} = \mathbf{F}^t \cdot \mathbf{h}, \quad (7.2)$$

$$\rho_{f0} = J_{\mathbf{F}} \rho_{ft}. \quad (7.3)$$

By making use of (3), (6), and (7) one arrives at the referential representation of Maxwell's equations,

$$\text{Gauss's electric law (referential)} \quad \int_{\partial \mathcal{B}_0} \mathbf{D} \cdot \mathbf{N} \, dA = \int_{\mathcal{B}_0} \rho_{f0} \, dV \quad (8.1)$$

$$\text{Gauss's magnetic law (referential)} \quad \int_{\partial \mathcal{B}_0} \mathbf{B} \cdot \mathbf{N} \, dA = 0 \quad (8.2)$$

$$\text{Faraday's law of induction (referential)} \quad \int_{\partial \mathcal{A}_0} \mathcal{E} \cdot d\mathbf{S} = -\frac{d}{dt} \int_{\mathcal{A}_0} \mathbf{B} \cdot \mathbf{N} \, dA \quad (8.3)$$

$$\text{Ampère's circuital law (referential)} \quad \int_{\partial \mathcal{A}_0} \mathcal{H} \cdot d\mathbf{S} = \int_{\mathcal{A}_0} \mathbf{J} \cdot \mathbf{N} \, dA + \frac{d}{dt} \int_{\mathcal{A}_0} \mathbf{D} \cdot \mathbf{N} \, dA. \quad (8.4)$$

In addition, by evaluating (8.4) for a closed surface and by inserting (8.1) in the ensuing equation one obtains the continuity equation for the electric current in referential form,

$$0 = \int_{\partial \mathcal{B}_0} \mathbf{J} \cdot \mathbf{N} \, dA + \frac{d}{dt} \int_{\mathcal{B}_0} \rho_{f0} \, dV, \quad (9)$$

with

$$i_0 = \mathbf{J} \cdot \mathbf{N} \quad (10)$$

denoting the projected current density vector. The localisation of (8) and (9) by making use of Gauss's theorem and Stoke's theorem eventually results in

$$\text{Gauss's electric law (referential)} \quad \nabla_{\mathbf{X}} \cdot \mathbf{D} = \rho_{f0}, \quad (11.1)$$

$$\text{Gauss's magnetic law (referential)} \quad \nabla_{\mathbf{X}} \cdot \mathbf{B} = 0, \quad (11.2)$$

$$\text{Faraday's law of induction (referential)} \quad \nabla_{\mathbf{X}} \times \mathcal{E} = -\dot{\mathbf{B}}, \quad (11.3)$$

$$\text{Ampère's circuital law (referential)} \quad \nabla_{\mathbf{X}} \times \mathcal{H} = \mathbf{J} + \dot{\mathbf{D}} \quad (11.4)$$

and

$$\nabla_{\mathbf{X}} \cdot \mathbf{J} + \dot{\rho}_{f0} = 0. \quad (12)$$

Under the assumption of a (quasi-)stationary state, Faraday's law of induction (11.3) simplifies and can naturally be fulfilled by the introduction of a scalar-valued potential ϕ for the (referential and spatial) Minkowskian electric field vectors,

$$\mathbf{E} = \mathbf{F}^t \cdot \mathbf{e}, \quad (13.1)$$

$$\mathbf{E} = -\nabla_{\mathbf{X}} \phi, \quad (13.2)$$

$$\mathbf{e} = -\nabla_{\mathbf{x}} \phi. \quad (13.3)$$

Accordingly, the electrical subproblem reduces to the continuity equation for the electric current density,

$$\nabla_{\mathbf{X}} \cdot \mathbf{J} = 0, \quad (14)$$

with Gauss's electric law (11.1) defining the local free charge density.

2.3 Conservation of energy and dissipation inequality

Taking into account mechanical, thermal, and electrical contributions and introducing the (mass-specific) internal energy density e , the balance equation of energy with respect to the spatial configuration is given by

$$\begin{aligned} \frac{d}{dt} \int_{\mathcal{B}_t} \rho_t e \, dv + \frac{d}{dt} \int_{\mathcal{B}_t} \frac{1}{2} \rho_t \dot{\mathbf{x}} \cdot \dot{\mathbf{x}} \, dv &= \int_{\mathcal{B}_t} \dot{\mathbf{x}} \cdot \rho_t \mathbf{f} \, dv + \int_{\partial \mathcal{B}_t} \dot{\mathbf{x}} \cdot \mathbf{t}_t \, da \\ &+ \int_{\mathcal{B}_t} \rho_t r \, dv - \int_{\partial \mathcal{B}_t} \mathbf{q} \cdot \mathbf{n} \, da + \int_{\mathcal{B}_t} \mathbf{j} \cdot \boldsymbol{\epsilon} \, dv \quad , \end{aligned} \quad (15)$$

with $\rho_t = \rho_0/J_{\mathbf{F}}$ denoting the mass density with respect to the current configuration, r denoting heat sources or sinks and with the spatial heat flux vector \mathbf{q} that is related to its referential counterpart $\mathbf{Q} = J_{\mathbf{F}} \mathbf{F}^{-1} \cdot \mathbf{q}$. The last summand on the right-hand side of (15) is related to the electrical subproblem with the scalar product of the electric current density vector and the electric field vector acting as a source term, cf. [8,9,34]. For the sake of simplicity, additional energy contributions associated with polarisation and magnetisation are neglected.

By following standard procedures, (15) can equivalently be expressed with respect to the reference configuration,

$$\begin{aligned} \frac{d}{dt} \int_{\mathcal{B}_0} \rho_0 e \, dV + \frac{d}{dt} \int_{\mathcal{B}_0} \frac{1}{2} \rho_0 \dot{\mathbf{x}} \cdot \dot{\mathbf{x}} \, dV &= \int_{\mathcal{B}_0} \dot{\mathbf{x}} \cdot \rho_0 \mathbf{f} \, dV + \int_{\partial \mathcal{B}_0} \dot{\mathbf{x}} \cdot \mathbf{t}_0 \, dA \\ &+ \int_{\mathcal{B}_0} \rho_0 r \, dV - \int_{\partial \mathcal{B}_0} \mathbf{Q} \cdot \mathbf{N} \, dA + \int_{\mathcal{B}_0} \mathbf{J} \cdot \boldsymbol{\mathcal{E}} \, dV, \end{aligned} \quad (16)$$

and localised as

$$\rho_0 \dot{e} = \mathbf{P} : \dot{\mathbf{F}} + \rho_0 r - \nabla_{\mathbf{X}} \cdot \mathbf{Q} + \mathbf{J} \cdot \boldsymbol{\mathcal{E}} \quad . \quad (17)$$

Furthermore, the localisation of the classic referential form of the dissipation inequality

$$\frac{d}{dt} \int_{\mathcal{B}_0} \rho_0 s \, dV \geq \int_{\mathcal{B}_0} \frac{\rho_0 r}{\theta} \, dV - \int_{\partial \mathcal{B}_0} \frac{\mathbf{Q} \cdot \mathbf{N}}{\theta} \, dA \quad , \quad (18)$$

with s denoting the (mass-specific) entropy density, yields

$$\mathbf{P} : \dot{\mathbf{F}} - \rho_0 [\dot{\psi} + s \dot{\theta}] - \frac{1}{\theta} \mathbf{Q} \cdot \nabla_{\mathbf{X}} \theta + \mathbf{J} \cdot \boldsymbol{\mathcal{E}} \geq 0 \quad . \quad (19)$$

In the derivation of (19), the convex–concave Legendre–(Fenchel) transformation with regard to the (mass specific) Helmholtz free energy density $\psi(\mathbf{F}, \theta, \bullet)$ was invoked in addition to (1) and (17). Moreover, it is observed that the flow of electric charges is, intrinsically, a dissipative process and that (19) poses restrictions on the particular form of the constitutive equation for the current density vector. The (dissipative) processes that are in the focus of the present contribution are thus significantly different from the (possibly reversible) processes of electro-active solids studied in e.g. [35].

3 Multiscale modelling

In computational multiscale methods, classic constitutive equations are substituted by a microscale boundary value problem, and effective macroscale quantities are calculated based on their microscopic counterparts by means of averaging theorems. In particular, a separation of time and length scales is assumed which motivates the assumption of negligible body forces [33,37]. Moreover, we restrict ourselves to quasi-stationary problems such that, based on (1) and (14), the electro-mechanically coupled microscale boundary value problem takes the form

$$\nabla_{\mathbf{X}_m} \cdot \mathbf{P}_m = \mathbf{0} \quad , \quad (20.1)$$

$$\nabla_{\mathbf{X}_m} \cdot \mathbf{J}_m = 0 \quad . \quad (20.2)$$

In (20) and in the following, superscripts \bullet_m and \bullet_M indicate micro- and macroscale quantities, respectively. The corresponding averaging theorems that relate quantities at the two length scales are discussed in Sect. 3.1.

These are closely related to the extended Hill–Mandel condition proposed in Sect. 3.2 which can a priori be fulfilled by the choice of boundary conditions as shown in Sect. 3.3. The ensuing derivations are based on and are direct extensions of well-established computational homogenisation procedures. For the mechanical subproblem, these are, for instance, discussed in [12, 24, 27, 28, 30]. Multifield-multiscale methods for thermo-mechanically coupled problems are moreover elaborated in e.g. [33] and applications to electro-mechanically coupled problems of dielectric solids are discussed in e.g. [35]. Focusing on electrical conductors, a multiscale method was recently proposed in [19] subject to the assumption of infinitesimal deformations.

3.1 Averaging theorems

In accordance with [3, 37], (referential) macroscopic quantities are defined in terms of (referential) volume averages of their microscopic counterparts. Furthermore, an alternative representation in terms of surface integrals is derived which turns out to be beneficial for the evaluation of the extended Hill–Mandel condition in Sect. 3.2 and for the derivation of algorithmic tangent stiffness contributions in Section 4.2.

More specifically speaking, by making use of the identity

$$\int_{\mathcal{B}_{0m}} \nabla_{\mathbf{X}_m} \bullet \, dV = \int_{\mathcal{B}_{0m}} [\nabla_{\mathbf{X}_m} \bullet] \cdot \mathbf{I}^t \, dV = \int_{\mathcal{B}_{0m}} \nabla_{\mathbf{X}_m} \cdot [\bullet \otimes \mathbf{I}] \, dV = \int_{\partial \mathcal{B}_{0m}} \bullet \otimes \mathbf{N}_m \, dA \quad (21)$$

and of the definition

$$V_m = \int_{\mathcal{B}_{0m}} dV \quad , \quad (22)$$

volume averages of the kinematic-type quantities can be expressed as

$$\mathbf{F}_M = \frac{1}{V_m} \int_{\mathcal{B}_{0m}} \mathbf{F}_m \, dV = \frac{1}{V_m} \int_{\mathcal{B}_{0m}} \nabla_{\mathbf{X}_m} \mathbf{x}_m \, dV = \frac{1}{V_m} \int_{\partial \mathcal{B}_{0m}} \mathbf{x}_m \otimes \mathbf{N}_m \, dA \quad , \quad (23)$$

$$\mathbf{E}_M = \frac{1}{V_m} \int_{\mathcal{B}_{0m}} \mathbf{E}_m \, dV = \frac{1}{V_m} \int_{\mathcal{B}_{0m}} -\nabla_{\mathbf{X}_m} \phi_m \, dV = \frac{1}{V_m} \int_{\partial \mathcal{B}_{0m}} -\phi_m \mathbf{N}_m \, dA \quad . \quad (24)$$

Their energetic duals

$$\mathbf{P}_M = \frac{1}{V_m} \int_{\mathcal{B}_{0m}} \mathbf{P}_m \, dV = \frac{1}{V_m} \int_{\partial \mathcal{B}_{0m}} \underbrace{\mathbf{P}_m \cdot \mathbf{N}_m}_{=\mathbf{t}_{0m}} \otimes \mathbf{X}_m \, dA - \frac{1}{V_m} \int_{\mathcal{B}_{0m}} \underbrace{[\nabla_{\mathbf{X}_m} \cdot \mathbf{P}_m]}_{=\mathbf{0}} \otimes \mathbf{X}_m \, dA \quad (25)$$

and

$$\begin{aligned} \mathbf{J}_M &= \frac{1}{V_m} \int_{\mathcal{B}_{0m}} \mathbf{J}_m \, dV = \frac{1}{V_m} \int_{\mathcal{B}_{0m}} \mathbf{J}_m \cdot [\nabla_{\mathbf{X}_m} \mathbf{X}_m]^t \, dV \\ &= \frac{1}{V_m} \int_{\mathcal{B}_{0m}} \nabla_{\mathbf{X}_m} \cdot [\mathbf{X}_m \otimes \mathbf{J}_m] \, dV - \frac{1}{V_m} \int_{\mathcal{B}_{0m}} [\nabla_{\mathbf{X}_m} \cdot \mathbf{J}_m] \mathbf{X}_m \, dV \\ &= \frac{1}{V_m} \int_{\partial \mathcal{B}_{0m}} \underbrace{\mathbf{J}_m \cdot \mathbf{N}_m}_{=i_{0m}} \otimes \mathbf{X}_m \, dA - \frac{1}{V_m} \int_{\mathcal{B}_{0m}} \underbrace{[\nabla_{\mathbf{X}_m} \cdot \mathbf{J}_m]}_{=0} \mathbf{X}_m \, dV \end{aligned} \quad (26)$$

follow by taking into account the set of balance equations (20). It is remarked that (25) and (26) may alternatively be derived by invoking (23), (24) and evaluating the Hill–Mandel energy equivalence conditions for specific kinematic boundary conditions.

3.2 Hill–Mandel conditions

Based on the balance equation of energy, (17), and in analogy with the well-established Hill–Mandel condition of a purely mechanical problem,

$$\mathbf{P}_M : \delta \mathbf{F}_M = \frac{1}{V_m} \int_{\mathcal{B}_{0m}} \mathbf{P}_m : \delta \mathbf{F}_m \, dV = \frac{1}{V_m} \int_{\partial \mathcal{B}_{0m}} \delta \mathbf{x}_m \cdot \underbrace{\mathbf{P}_m \cdot \mathbf{N}_m}_{=\mathbf{t}_{0m}} \, dA - \frac{1}{V_m} \int_{\mathcal{B}_{0m}} \delta \mathbf{x}_m \cdot \underbrace{[\nabla_{\mathbf{X}_m} \cdot \mathbf{P}_m]}_{=\mathbf{0}} \, dV, \quad (27)$$

the micro-macro energy equivalence condition

$$\begin{aligned} \mathbf{J}_M \cdot \delta \mathbf{E}_M &= \frac{1}{V_m} \int_{\mathcal{B}_{0m}} \mathbf{J}_m \cdot \delta \mathbf{E}_m \, dV = -\frac{1}{V_m} \int_{\mathcal{B}_{0m}} \mathbf{J}_m \cdot \nabla_{\mathbf{X}_m} \delta \phi_m \, dV \\ &= -\frac{1}{V_m} \int_{\mathcal{B}_{0m}} \nabla_{\mathbf{X}_m} \cdot [\delta \phi_m \mathbf{J}_m] \, dV + \frac{1}{V_m} \int_{\mathcal{B}_{0m}} \delta \phi_m [\nabla_{\mathbf{X}_m} \cdot \mathbf{J}_m] \, dV \\ &= -\frac{1}{V_m} \int_{\partial \mathcal{B}_{0m}} \delta \phi_m \underbrace{\mathbf{J}_m \cdot \mathbf{N}_m}_{=i_{0m}} \, dA + \frac{1}{V_m} \int_{\mathcal{B}_{0m}} \delta \phi_m \underbrace{[\nabla_{\mathbf{X}_m} \cdot \mathbf{J}_m]}_{=0} \, dV \end{aligned} \quad (28)$$

is additionally accounted for.

3.3 Boundary conditions

Mechanical and electrical RVE boundary conditions that can be shown to be consistent with the scale bridging relations (23)–(26) and to fulfil the Hill–Mandel conditions (27) and (28) are summarised in (29):

	mechanical	electrical	
affine	$\mathbf{x}_m = \mathbf{F}_M \cdot \mathbf{X}_m$	$\phi_m = \phi_M - \mathbf{E}_M \cdot \mathbf{X}_m,$	(29.1)

periodic	$[\mathbf{x}_m^+ - \mathbf{x}_m^-] = \mathbf{F}_M \cdot [\mathbf{X}_m^+ - \mathbf{X}_m^-]$	$[\phi_m^+ - \phi_m^-] = -\mathbf{E}_M \cdot [\mathbf{X}_m^+ - \mathbf{X}_m^-],$	(29.2)
----------	--	--	--------

	$\mathbf{t}_{0m}^+ = -\mathbf{t}_{0m}^-$	$i_{0m}^+ = -i_{0m}^-,$	(29.3)
--	--	-------------------------	--------

uniform flux	$\mathbf{t}_{0m} = \mathbf{P}_M \cdot \mathbf{N}_m$	$i_{0m} = \mathbf{J}_M \cdot \mathbf{N}_m$	(29.4)
--------------	---	--	--------

with superscripts \bullet^+ and \bullet^- referring to quantities at two opposing parts of the RVE-boundary. Since comprehensive discussions of boundary conditions for the mechanical subproblem are available in the literature, see e.g. [37], the subsequent discussion is restricted to the suitability of the electrical boundary conditions.

With regard to the affine boundary conditions of the electrical problem (29.1) and in view of (20), (24), (26), and (28), it is observed that

$$\begin{aligned} \frac{1}{V_m} \int_{\mathcal{B}_{0m}} \mathbf{E}_m \, dV &= \frac{1}{V_m} \int_{\partial \mathcal{B}_{0m}} -[\phi_M - \mathbf{E}_M \cdot \mathbf{X}_m] \mathbf{N}_m \, dA \\ &= \frac{1}{V_m} \int_{\mathcal{B}_{0m}} \nabla_{\mathbf{X}_m} \cdot [-[\phi_M - \mathbf{E}_M \cdot \mathbf{X}_m] \mathbf{I}] \, dV = \mathbf{E}_M \end{aligned} \quad (30)$$

and that

$$\begin{aligned} \frac{1}{V_m} \int_{\mathcal{B}_{0m}} \mathbf{J}_m \cdot \delta \mathbf{E}_m \, dV &= -\frac{1}{V_m} \int_{\partial \mathcal{B}_{0m}} i_{0m} [\delta \phi_M - \delta \mathbf{E}_M \cdot \mathbf{X}_m] \, dA \\ &= \frac{1}{V_m} \int_{\partial \mathcal{B}_{0m}} i_{0m} \mathbf{X}_m \, dA \cdot \delta \mathbf{E}_M = \mathbf{J}_M \cdot \delta \mathbf{E}_M \end{aligned} \quad (31)$$

hold.

Likewise, taking into account the (anti-)periodicity conditions (29.2) and (29.3) in addition to the geometric constraint for outward unit surface normal vectors,

$$\mathbf{N}_m^+ = -\mathbf{N}_m^-, \quad (32)$$

one arrives at

$$\begin{aligned} \frac{1}{V_m} \int_{\mathcal{B}_{0m}} \mathbf{E}_m \, dV &= -\frac{1}{V_m} \left[\int_{\partial\mathcal{B}_{0m}^+} \phi_m^+ \mathbf{N}_m^+ \, dA + \int_{\partial\mathcal{B}_{0m}^-} \phi_m^- \mathbf{N}_m^- \, dA \right] \\ &= \frac{1}{V_m} \left[\int_{\partial\mathcal{B}_{0m}^+} \mathbf{E}_M \cdot [\mathbf{X}_m^+ - \mathbf{X}_m^-] \otimes \mathbf{N}_m^+ \, dA \right] \\ &= \frac{1}{V_m} \left[\mathbf{E}_M \cdot \int_{\partial\mathcal{B}_{0m}} \mathbf{X}_m \otimes \mathbf{I} \cdot \mathbf{N}_m \, dA \right] = \mathbf{E}_M \end{aligned} \quad (33)$$

and

$$\begin{aligned} \frac{1}{V_m} \int_{\mathcal{B}_{0m}} \mathbf{J}_m \cdot \delta\mathbf{E}_m \, dV &= -\frac{1}{V_m} \left[\int_{\partial\mathcal{B}_{0m}^+} i_{0m}^+ \delta\phi_m^+ \, dA + \int_{\partial\mathcal{B}_{0m}^-} i_{0m}^- \delta\phi_m^- \, dA \right] \\ &= \frac{1}{V_m} \left[\int_{\partial\mathcal{B}_{0m}^+} i_{0m}^+ [\delta\mathbf{E}_M \cdot [\mathbf{X}_m^+ - \mathbf{X}_m^-]] \, dA \right] \\ &= \frac{1}{V_m} \left[\int_{\partial\mathcal{B}_{0m}} i_{0m} \mathbf{X}_m \, dA \cdot \delta\mathbf{E}_M \right] = \mathbf{J}_M \cdot \delta\mathbf{E}_M. \end{aligned} \quad (34)$$

Finally, by evaluating (26) for (29.4) one arrives at

$$\frac{1}{V_m} \int_{\mathcal{B}_{0m}} \mathbf{J}_m \, dV = \frac{1}{V_m} \int_{\partial\mathcal{B}_{0m}} \mathbf{X}_m \otimes \mathbf{J}_M \cdot \mathbf{N}_m \, dA - \frac{1}{V_m} \int_{\mathcal{B}_{0m}} [\nabla_{\mathbf{X}_m} \cdot \mathbf{J}_M] \mathbf{X}_m \, dV = \mathbf{J}_M, \quad (35)$$

and by evaluating (28) for (29.4) at

$$\frac{1}{V_m} \int_{\mathcal{B}_{0m}} \mathbf{J}_m \cdot \delta\mathbf{E}_m \, dV = -\frac{1}{V_m} \int_{\partial\mathcal{B}_{0m}} \delta\phi_m \mathbf{J}_M \cdot \mathbf{N}_m \, dA = \mathbf{J}_M \cdot \left[-\frac{1}{V_m} \int_{\partial\mathcal{B}_{0m}} \delta\phi_m \mathbf{N}_m \, dA \right] = \mathbf{J}_M \cdot \delta\mathbf{E}_M. \quad (36)$$

4 Finite element implementation

Based on the theoretical fundamentals presented in Sects. 2 and 3, this Section focuses on the finite element-based solution of electro-mechanically coupled multiscale problems for affine and periodic boundary conditions at the microscale. In particular, discrete representations of the averaging theorems (25) and (26) are discussed in Sect. 4.1, and the corresponding tangent stiffness contributions that are required in an iterative, gradient-based solution procedure at the macroscale are derived in Sect. 4.2. For the purely mechanical case, these numerical procedures are well established and, for instance, discussed in the pioneering work [27]. Extensions to thermo-mechanically coupled problems and to electro-mechanically coupled problems of dielectric solids are discussed in e.g. [20,21,33,37].

For affine boundary conditions, the subsequent derivations are based on the generalised stiffness matrix \mathbf{K}_m and on the generalised reaction force vector \mathbf{f}_m . In the case of periodic boundary conditions, the latter quantities need to be substituted by the reduced generalised stiffness matrix \mathbf{K}_m^* and by the reduced generalised reaction force vector \mathbf{f}_m^* that occur when enforcing (anti-)periodicity conditions via linear constraints, e.g. [40]. More specifically speaking, in each iteration the linear system

$$\mathbf{K}_m \cdot \Delta\mathcal{X}_m = \Delta\mathbf{f}_m \quad (37)$$

is partitioned into dependent \mathcal{X}_{md} and independent \mathcal{X}_{mi} degrees of freedom that are related via the transformation matrix \mathcal{T} according to

$$\mathbf{K}_m^* = \mathcal{T}^t \cdot \mathbf{K}_m \cdot \mathcal{T}, \quad \mathbf{f}_m^* = \mathcal{T}^t \cdot \mathbf{f}_m, \quad \begin{bmatrix} \mathcal{X}_{mi} \\ \mathcal{X}_{md} \end{bmatrix} = \mathcal{T} \cdot \mathcal{X}_{mi}, \quad (38)$$

and the reduced system

$$\mathbf{K}_m^* \cdot \Delta\mathcal{X}_{mi} = \Delta\mathbf{f}_m^* \quad (39)$$

is solved.

4.1 Homogenisation

Scale-bridging relations in the proposed finite element implementation are based on (25) and (26), with occurring integrals being substituted by a sum over all n_{pn} Dirichlet nodes. In this regard, nodal quantities are indicated by superscripts (i) \bullet , and additional superscripts \bullet^φ and \bullet^ϕ are introduced to differ between mechanical and electrical contributions to the generalised (nodal) reaction force vector. With these definitions at hand, the discrete representations of (25) and (26) read

$$\mathbf{P}_M = \frac{1}{V_m} \int_{\partial \mathcal{B}_{0m}} \mathbf{t}_{0m} \otimes \mathbf{X}_m \, dA \approx \frac{1}{V_m} \sum_{i=1}^{n_{\text{pn}}} (i) \mathbf{f}_m^\varphi \otimes (i) \mathbf{X}_m \quad (40)$$

and

$$\mathbf{J}_M = \frac{1}{V_m} \int_{\partial \mathcal{B}_{0m}} i_{0m} \mathbf{X}_m \, dA \approx \frac{1}{V_m} \sum_{i=1}^{n_{\text{pn}}} (i) f_m^\phi (i) \mathbf{X}_m \quad (41)$$

4.2 Generalised algorithmic tangent stiffness tensors

In order to derive consistent algorithmic tangent stiffness operators, the linear system (37) is partitioned into Dirichlet \mathcal{X}_{mp} and free \mathcal{X}_{mf} degrees of freedom,

$$\begin{bmatrix} \mathbf{K}_{\text{mpp}} & \mathbf{K}_{\text{mpf}} \\ \mathbf{K}_{\text{mfp}} & \mathbf{K}_{\text{mff}} \end{bmatrix} \cdot \begin{bmatrix} \Delta \mathcal{X}_{\text{mp}} \\ \Delta \mathcal{X}_{\text{mf}} \end{bmatrix} = \begin{bmatrix} \Delta \mathbf{f}_{\text{mp}} \\ \mathbf{0} \end{bmatrix} \quad (42)$$

and the closed-form expression

$$\widehat{\mathbf{K}}_m \cdot \Delta \mathcal{X}_{\text{mp}} = \Delta \mathbf{f}_{\text{mp}} \quad , \quad \widehat{\mathbf{K}}_m = \mathbf{K}_{\text{mpp}} - \mathbf{K}_{\text{mpf}} \cdot \mathbf{K}_{\text{mff}}^{-1} \cdot \mathbf{K}_{\text{mfp}} \quad (43)$$

relating changes in the generalised reaction force vector to changes in the prescribed degrees of freedom is used. In the case of affine and periodic boundary conditions, the prescribed degrees of freedom are related to changes in the macroscopic mechanical and electrical field quantities according to

$$\Delta (j) \mathbf{x}_{\text{mp}} = \Delta \mathbf{F}_M \cdot (j) \mathbf{X}_m \quad (44)$$

and

$$\Delta (j) \phi_{\text{mp}} = \Delta \phi_M - \Delta \mathbf{E}_M \cdot (j) \mathbf{X}_m \quad (45)$$

Moreover, by partitioning (43) into mechanical and electrical contributions, indicated by superscript \bullet^φ and \bullet^ϕ , and by inserting (44) and (45) into the ensuing equation one arrives at

$$\Delta \mathbf{f}_m^{(i)\varphi} = \sum_{j=1}^{n_{pn}} (ij) \widehat{\mathbf{K}}_m^{\varphi\varphi} \cdot \Delta \mathbf{x}_{mp}^{(j)} + \sum_{j=1}^{n_{pn}} (ij) \widehat{\mathbf{K}}_m^{\varphi\phi} \Delta \phi_{mp}^{(j)} \quad (46.1)$$

$$= \sum_{j=1}^{n_{pn}} (ij) \widehat{\mathbf{K}}_m^{\varphi\varphi} \cdot \Delta \mathbf{F}_M \cdot \mathbf{X}_m^{(j)} - \sum_{j=1}^{n_{pn}} (ij) \widehat{\mathbf{K}}_m^{\varphi\phi} \otimes \Delta \mathbf{E}_M \cdot \mathbf{X}_m^{(j)} \quad (46.2)$$

and

$$\Delta f_m^{(i)\phi} = \sum_{j=1}^{n_{pn}} (ij) \widehat{\mathbf{K}}_m^{\phi\phi} \cdot \Delta \mathbf{x}_{mp}^{(j)} + \sum_{j=1}^{n_{pn}} (ij) \widehat{\mathbf{K}}_m^{\phi\phi} \Delta \phi_{mp}^{(j)} \quad (47.1)$$

$$= \sum_{j=1}^{n_{pn}} (ij) \widehat{\mathbf{K}}_m^{\phi\phi} \cdot \Delta \mathbf{F}_M \cdot \mathbf{X}_m^{(j)} - \sum_{j=1}^{n_{pn}} (ij) \widehat{\mathbf{K}}_m^{\phi\phi} \Delta \mathbf{E}_M \cdot \mathbf{X}_m^{(j)} \quad (47.2)$$

At this stage, it was used that the constitutive equations of the electro-mechanically coupled problem under consideration depend on the electric potential field only via its gradient, i.e. the electric field vector, such that changes in ϕ_M were neglected in (46) and (47) and will be neglected in the following. Finally, by inserting (46) into (40) one arrives at

$$\Delta \mathbf{P}_M \approx \underbrace{\frac{1}{V_m} \sum_{i=1}^{n_{pn}} \sum_{j=1}^{n_{pn}} (ij) \widehat{\mathbf{K}}_m^{\varphi\varphi} \otimes \left[\mathbf{X}_m^{(i)} \otimes \mathbf{X}_m^{(j)} \right]}_{= \frac{d\mathbf{P}_M}{d\mathbf{F}_M}} : \Delta \mathbf{F}_M - \underbrace{\frac{1}{V_m} \sum_{i=1}^{n_{pn}} \sum_{j=1}^{n_{pn}} (ij) \widehat{\mathbf{K}}_m^{\varphi\phi} \otimes \mathbf{X}_m^{(i)} \otimes \mathbf{X}_m^{(j)} \cdot \Delta \mathbf{E}_M}_{= \frac{d\mathbf{P}_M}{d\mathbf{E}_M}}, \quad (48)$$

and by inserting (47) into (41) at

$$\Delta \mathbf{J}_M \approx \underbrace{\frac{1}{V_m} \sum_{i=1}^{n_{pn}} \sum_{j=1}^{n_{pn}} \mathbf{X}_m^{(i)} \otimes (ij) \widehat{\mathbf{K}}_m^{\phi\phi} \otimes \mathbf{X}_m^{(j)}}_{= \frac{d\mathbf{J}_M}{d\mathbf{F}_M}} : \Delta \mathbf{F}_M - \underbrace{\frac{1}{V_m} \sum_{i=1}^{n_{pn}} \sum_{j=1}^{n_{pn}} (ij) \widehat{\mathbf{K}}_m^{\phi\phi} \mathbf{X}_m^{(i)} \otimes \mathbf{X}_m^{(j)} \cdot \Delta \mathbf{E}_M}_{= \frac{d\mathbf{J}_M}{d\mathbf{E}_M}}. \quad (49)$$

5 Representative simulation results

This Section focuses on the study of representative boundary value problems so as to reveal the influence of mechanically induced microscale deformation processes on effective (electrical) macroscale material properties. To this end, the microscale material model is briefly summarised in Sect. 5.1, and sample boundary value problems in two- and three-dimensional settings are studied in Sects. 5.2 and 5.3.

5.1 Microscale material models

At the microscale, the Neo-Hookean-type energy potential,

$$\tilde{\Psi}(\mathbf{F}) = \rho_0 \tilde{\psi}(\mathbf{F}) = \lambda \frac{J_{\mathbf{F}}^2 - 1}{4} - \left[\frac{\lambda}{2} + \mu \right] \ln(J_{\mathbf{F}}) + \frac{1}{2} \mu [\mathbf{F} : \mathbf{F} - 3], \quad (50)$$

is adopted, featuring material parameters λ and μ that are akin to the Lamé constants of a small strain theory. In virtue of (19), (50) gives rise to the specific form of the Piola stress tensor:

$$\mathbf{P} = \frac{\lambda}{2} [J_{\mathbf{F}}^2 - 1] \mathbf{F}^{-t} + \mu [\mathbf{F} - \mathbf{F}^{-t}], \quad (51)$$

Table 1 Material parameters of an idealised material used in the simulations

E	ν	κ_t
130000 N/mm ²	0.35	58100 A/[Vmm]

with associated tangent stiffness contributions

$$\frac{d\mathbf{P}}{d\mathbf{F}} = \lambda J_{\mathbf{F}}^2 \mathbf{F}^{-t} \otimes \mathbf{F}^{-t} - \left[\frac{\lambda}{2} [J_{\mathbf{F}}^2 - 1] - \mu \right] \mathbf{F}^{-t} \underline{\otimes} \mathbf{F}^{-t} + \mu \mathbf{I} \underline{\otimes} \mathbf{I} \quad (52)$$

and

$$\frac{d\mathbf{P}}{d\mathbf{E}} = \mathbf{0} \quad (53)$$

In accordance with the restrictions on the electric current density vector posed by (19), a linear relation between the (spatial) electric current density vector and the (spatial) electric field vector is adopted at the microscale, namely

$$\mathbf{j} = \mathcal{S}_t \cdot \mathbf{e} \quad (54)$$

In (54), \mathcal{S}_t denotes the positive (semi-)definite spatial conductivity tensor that is chosen to be constant, isotropic, and to depend on the scalar-valued conductivity parameter κ_t , namely

$$\mathcal{S}_t = \kappa_t \mathbf{I} \quad (55)$$

Assuming κ_t to be constant allows us to study the influence of finite geometry changes at the microscale (e.g. of voids) on the effective electrical conductivity tensor at the macroscale. In this regard, taking κ_t to be constant is a simplifying modelling assumption. Regarding for example metals, irreversible plastic deformation processes would be associated with the finite deformations studied in the present contribution. These would, in turn, be accompanied by an increase in dislocation density which is expected to influence the electrical conductivity as discussed in e.g. [1,4,15].

By additionally invoking (6.1) and (6.3), the referential representation of (54) follows as

$$\mathbf{J} = [J_{\mathbf{F}} \mathbf{F}^{-1} \cdot \mathcal{S}_t \cdot \mathbf{F}^{-t}] \cdot \mathbf{E} \quad (56)$$

with tangent stiffness contributions

$$\frac{d\mathbf{J}}{d\mathbf{E}} = J_{\mathbf{F}} \mathbf{F}^{-1} \cdot \mathcal{S}_t \cdot \mathbf{F}^{-t} \quad (57)$$

and

$$\frac{d\mathbf{J}}{d\mathbf{F}} = -J_{\mathbf{F}} \mathbf{F}^{-1} \otimes \mathbf{F}^{-1} \cdot \mathcal{S}_t \cdot \mathbf{F}^{-t} \cdot \mathbf{E} - J_{\mathbf{F}} \mathbf{F}^{-1} \cdot [[\mathcal{S}_t \otimes \mathbf{F}^{-t}] \underline{\otimes} \mathbf{F}^{-t}] \cdot \mathbf{E} + J_{\mathbf{F}} \mathbf{F}^{-1} \cdot \mathcal{S}_t \cdot \mathbf{F}^{-t} \cdot \mathbf{E} \otimes \mathbf{F}^{-t}. \quad (58)$$

5.2 Two-dimensional representative simulations

In this Section, the influence of mechanically induced deformation processes on the electrical conductivity is studied in a two-dimensional plane strain setting. In particular, focus is on the biaxial tensile test specimen depicted in Fig. 1a. The specimen is assumed to consist of two different materials as indicated in light and dark grey. In the dark grey-coloured region, a material microstructure with a circular void according to Fig. 1b is assumed, and the effective macroscopic material behaviour is calculated by using the multifield multiscale formulation proposed in this contribution. In the light grey-coloured region, an idealised material behaviour representing a microstructure without voids is assumed. The respective material parameters are summarised in Table 1.

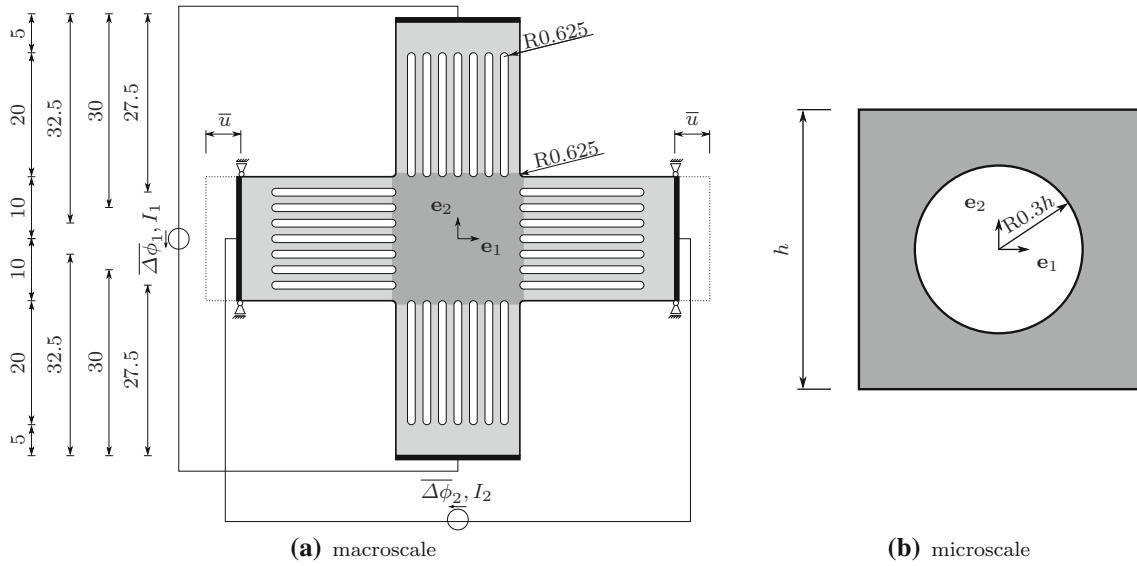


Fig. 1 a Biaxial tensile test specimen used in the electro-mechanically coupled multiscale simulations. Microstructural imperfections according to **b** are assumed in the dark grey-coloured region and resolved by using the proposed multiscale approach. In the light grey-coloured region, a classic phenomenological material model is used. Dimensions are given in mm

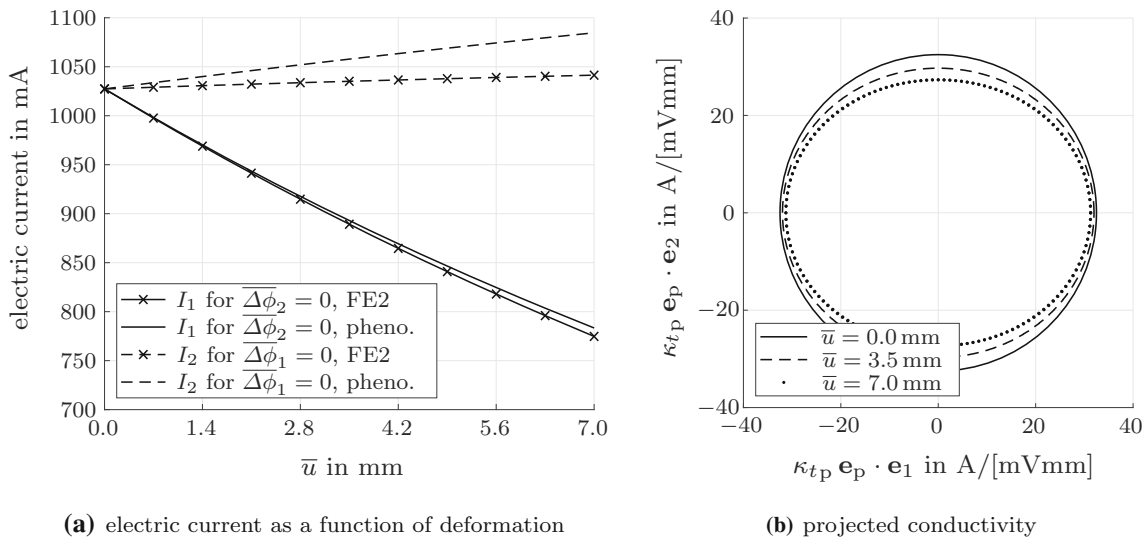


Fig. 2 a Electric current I_\bullet (surface integral of projected electric current density vector i_0) as a function of deformation for a prescribed electric potential difference $\Delta\phi_\bullet = 0.1$ mV, see Fig. 1. Curves labelled with “FE2” indicate fully coupled electro-mechanical multiscale simulations. Curves labelled with “pheno.” indicate reference solutions with a multiscale approach used for the mechanical problem and a classic phenomenological material model with a constant spatial conductivity tensor used for the electrical problem. Stated differently, in the latter case the inhomogeneous deformation of the microstructure is only accounted for in the evaluation of the mechanical problem. b Evolution of the spatial conductivity tensor near the centre of the specimen. For each deformation state, given in terms of the prescribed displacement \bar{u} , the distance of points to the origin represents the projected conductivity κ_{tp} in the respective spatial direction \mathbf{e}_p

The biaxial tensile test specimen is loaded in \mathbf{e}_1 -direction, with the prescribed horizontal displacement \bar{u} being linearly increased and the vertical displacement enforced to be zero at both ends. The remaining boundaries are assumed to be traction-free. Regarding the electrical subproblem, either a potential difference $\Delta\phi_1$ or a potential difference $\Delta\phi_2$ is prescribed. The remaining boundaries are assumed to be electrically insulated, i.e. $\mathbf{J} \cdot \mathbf{N} = 0$ holds. From a numerical point of view, four-node quadrilateral elements and a Gaussian integration scheme featuring four sampling points are used at the micro- and at the macroscale. Moreover, periodic boundary conditions are assumed at the microscale.

A reference model is introduced in order to evaluate the influence of the microscale deformation on the effective macroscopic quantities that may be measured in experiments. This model does not take changes in the effective conductivity tensor due to deformation processes at the microscale into account. However, the mechanical behaviour is still assumed to be governed by the microscale so that the macroscopic deformation is the same as in the complete FE²-model. To this end, the FE²-based calculation of the electrical subproblem in the dark grey-coloured region is replaced by a classic single-scale material model with the effective spatial conductivity tensor

$$\tilde{\mathcal{S}}_t = \tilde{\kappa}_t \mathbf{I} \quad \text{with} \quad \tilde{\kappa}_t = 32\,488.9 \text{ A/[Vmm]} \quad (59)$$

that resembles the properties of the microstructure in the undeformed state. The respective elongation–electric current curves are provided in Fig. 2a: 1) By comparing the $\Delta\phi_1 = 0.1 \text{ mV}$ and $\Delta\phi_2 = 0.1 \text{ mV}$ curves, a significant difference in the electric current is observed that can primarily be attributed to the macroscopic deformation process. In particular, the effective electrical resistance in \mathbf{e}_1 -direction increases because the length of the specimen increases while the effective cross section is reduced. Likewise, the effective electrical resistance in \mathbf{e}_2 -direction decreases. 2) Regarding the difference between FE²-based simulations (that account for the influence of the inhomogeneous microscale deformation on the effective macroscopic conductivity tensor) and the reference model as defined above (that does not account for deformation-induced changes in the conductivity tensor), one observes a significant decrease in the electric current with increasing deformation for the complete FE² model. Stated differently, the coefficients of the homogenised spatial macroscopic conductivity tensor

$$\mathcal{S}_{tM} = \frac{1}{J_{FM}} \mathbf{F}_M \cdot \frac{d\mathbf{J}_M}{d\mathbf{E}_M} \cdot \mathbf{F}_M^t \quad (60)$$

decrease with increasing deformation, for the deformation states analysed. The latter observation is further underlined by the directional conductivities

$$\kappa_{tp} = \left[\mathbf{e}_p \cdot \mathcal{S}_{tM}^{-1} \cdot \mathbf{e}_p \right]^{-1}, \quad (61)$$

depicted in Fig. 2b, which indicate a significant reduction in the effective macroscopic conductivity in \mathbf{e}_2 -direction, whereas only a moderate reduction in the conductivity in \mathbf{e}_1 -direction is observable. The projected conductivities are defined analogous to the directional Young's moduli of mechanical problems and emulate an uni-axial electric current in the respective spatial direction \mathbf{e}_p . The latter findings are further underlined by the deformed macro- and microscale configurations and the electric current density distributions depicted in Fig. 3. In particular, it is observed that a quasi-homogeneous state is achieved in the centre region of the chosen specimen. In addition to the results presented in this Section, the influence of the discretisation of the representative volume elements on the simulation results is briefly discussed in the [Appendix](#).

5.3 Three-dimensional representative simulations

In order to study the influence of mechanically induced deformation processes at the microscale on the effective macroscopic conductivity in a three-dimensional setting, uni-axial tension tests and simple shear tests are analysed. The macroscale boundary value problems are sketched in Fig. 4a, b. In the case of the uni-axial tension test, the boundary conditions are chosen such that the lateral contraction in \mathbf{e}_3 -direction is not hindered, whereas the displacements in \mathbf{e}_3 -direction are suppressed in the case of the simple shear test. Moreover, the prescribed displacement \bar{u} is linearly increased to $0.4h$. The material response at the macroscale is governed by the microstructure sketched in Fig. 4c that features a spherical void with a radius of 0.3 edge length. The microscale boundary value problem is based on the constitutive equations summarised in Sect. 5.1, and material parameters according to Table 1 are chosen. From a numerical point of view, 8-node hexahedral elements and a Gaussian quadrature scheme with eight sampling points are employed. Moreover, the microscale calculations are based on periodic boundary conditions.

The evolution of the effective macroscopic conductivity tensor as a function of deformation is visualised in Fig. 5 for the tensile test and in Fig. 6 for the simple shear test. In the case of the tensile test, no significant change of the directional conductivity in loading direction (\mathbf{e}_1 -direction) with increasing deformation is observed, whereas significant reductions in the directional conductivities in the \mathbf{e}_2 – \mathbf{e}_3 -plane are observed. Moreover, the

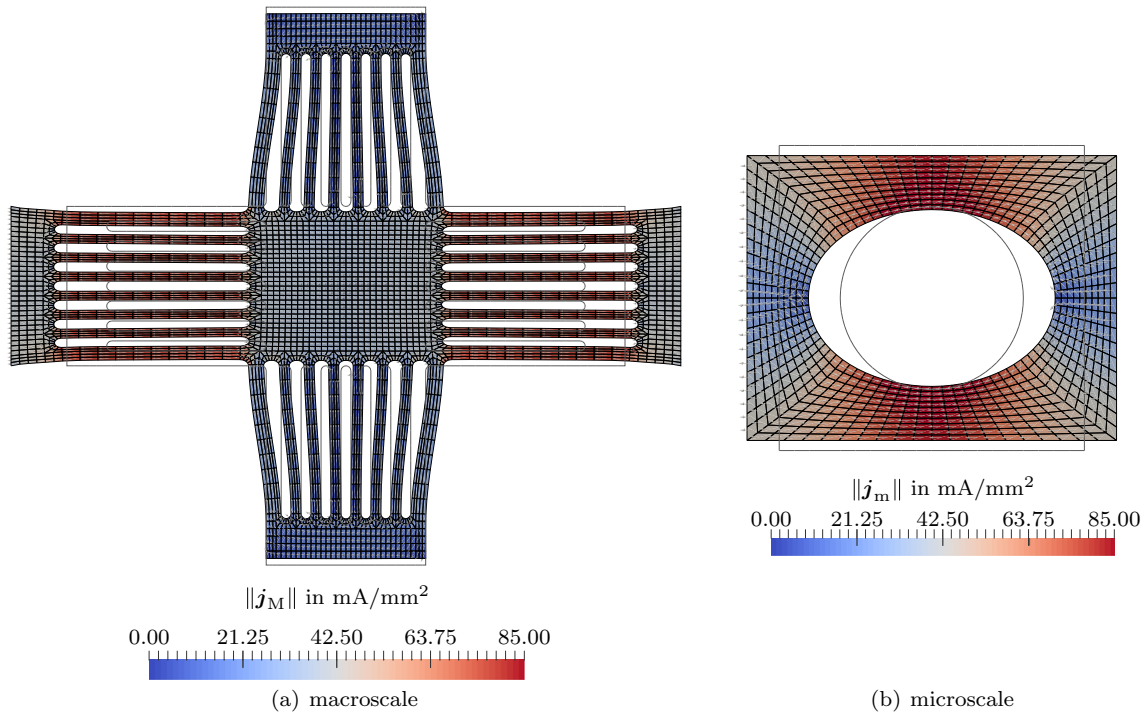


Fig. 3 Deformation and electric current density for the biaxial tensile test specimen according to Fig. 1 with $\bar{u} = 7.0$ mm, $\Delta\phi_1 = 0.1$ mV and $\Delta\phi_2 = 0.0$ mV. The outline of the reference configuration is depicted in light grey colour and the deformation of the microstructure shown for a quadrature point close to the centre of the specimen. Grey-coloured arrows indicate the direction of the electric current

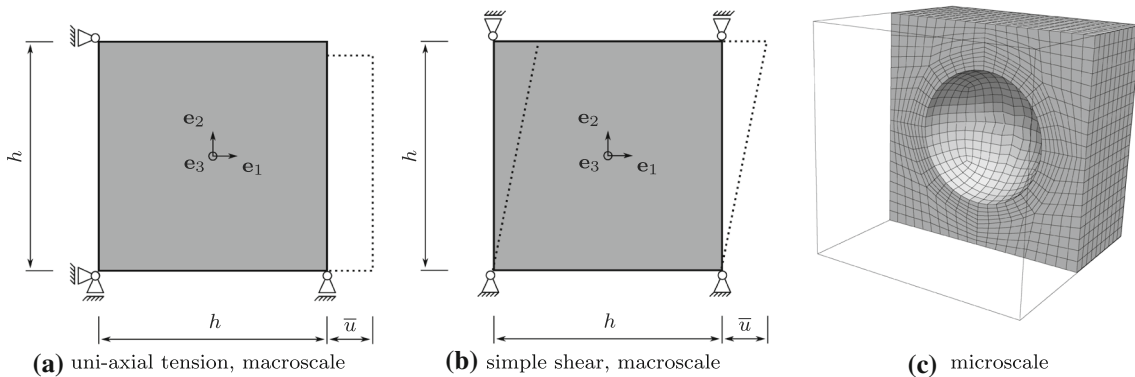


Fig. 4 a, b Three-dimensional macroscale boundary value problems. **c** Sectional view of FE-discretised microstructure featuring a spherical void with a radius of 0.3 edge length

principal axes of the (spatial) conductivity tensor are found to align with the loading direction and the \mathbf{e}_2 – \mathbf{e}_3 -plane. These observations are in good accordance with the two-dimensional simulation results discussed in Sect. 5.2 but significantly differ from those of the simple shear test visualised in Fig. 6. In the case of the simple shear test, the two principal axes of the spatial conductivity tensor in the \mathbf{e}_1 – \mathbf{e}_2 -plane are deformation dependent, with one eigenvalue increasing and one eigenvalue decreasing. The third principal axis is aligned with the \mathbf{e}_3 -direction. The corresponding eigenvalue of the spatial conductivity tensor slightly increases with the deformation.

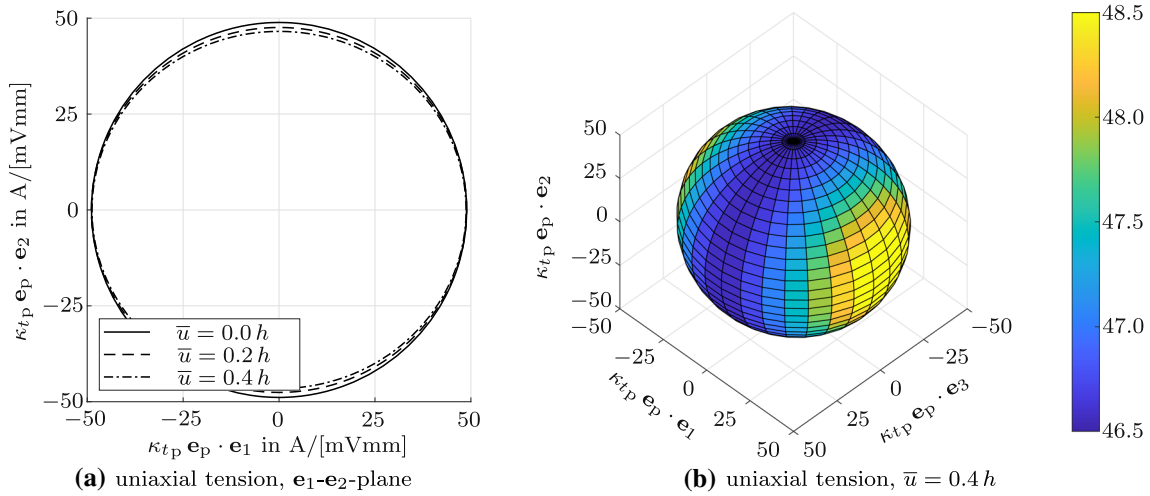


Fig. 5 Directional conductivities according to (61) for the three-dimensional uni-axial tensile test sketched in Fig. 4a

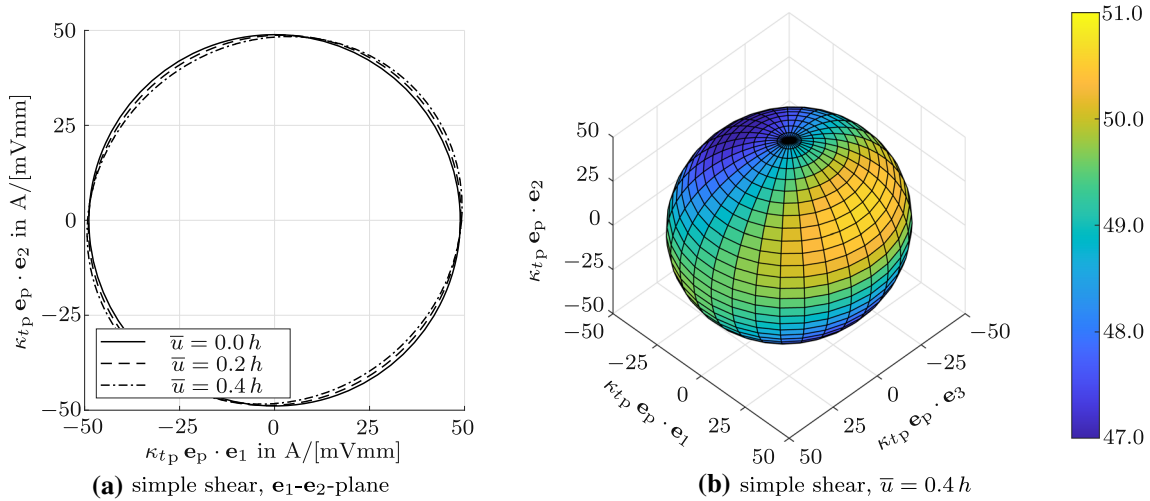


Fig. 6 Directional conductivities according to (61) for the three-dimensional simple shear test sketched in Fig. 4b

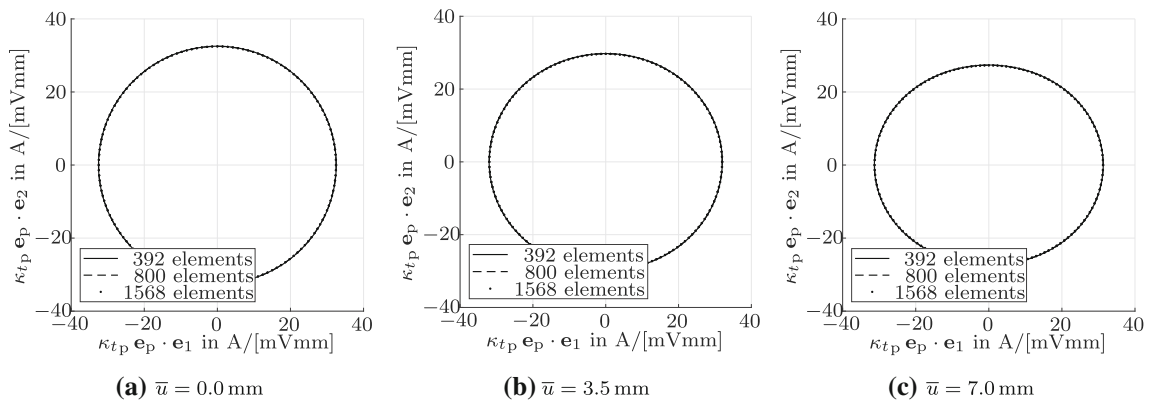


Fig. 7 Evolution of the spatial conductivity tensor near the centre of the specimen depicted in Fig. 1 for different representative volume element discretisations. For each deformation state, given in terms of the prescribed displacement \bar{u} , the distance of points to the origin represents the projected conductivity κ_{tp} in the respective spatial direction \mathbf{e}_p

6 Concluding remarks

Motivated by the fundamental theoretical developments on electro-mechanically coupled multiscale formulations for electrical conductors presented in [19], this contribution focused on the thermodynamically consistent extension of the proposed framework to a finite deformation setting. In particular, the set of partial differential equations governing the electro-mechanically coupled behaviour of electrical conductors in a finite strain setting was discussed, and appropriate scale bridging relations were proposed that are in accordance with well-established computational homogenisation procedures for mechanical problems, thermal problems, and electrical problems of dielectric solids. In addition, a finite element-based implementation of the multiscale framework was presented, and representative boundary value problems were studied in two- and three-dimensional settings. More specifically speaking, the analysis of a biaxial tensile test specimen in a two-dimensional setting revealed a severe influence of mechanically induced microscale deformations on the effective material properties at the macroscale. These findings were further underlined by a study of three-dimensional uni-axial tensile and simple shear tests where a deformation-induced evolution of the macroscale conductivity tensor could be observed.

The fundamental developments presented in this contribution provide a basis for the understanding of the influence of deformation processes, and especially of deformation-induced damage processes at the microscale on effective electrical material properties at the macroscale. Combined with more elaborated, irreversible microscale material models these developments are expected to eventually contribute to the development of non-destructive testing methods in the future.

Acknowledgements Funded by the Deutsche Forschungsgemeinschaft (DFG, German Research Foundation)—Project-ID 278868966—TRR 188.

Funding Open Access funding enabled and organized by Projekt DEAL.

Open Access This article is licensed under a Creative Commons Attribution 4.0 International License, which permits use, sharing, adaptation, distribution and reproduction in any medium or format, as long as you give appropriate credit to the original author(s) and the source, provide a link to the Creative Commons licence, and indicate if changes were made. The images or other third party material in this article are included in the article's Creative Commons licence, unless indicated otherwise in a credit line to the material. If material is not included in the article's Creative Commons licence and your intended use is not permitted by statutory regulation or exceeds the permitted use, you will need to obtain permission directly from the copyright holder. To view a copy of this licence, visit <http://creativecommons.org/licenses/by/4.0/>.

Declaration

Conflict of interest On behalf of all authors, the corresponding author states that there is no conflict of interest.

Appendix: Influence of the finite element discretisation

In this Appendix, the influence of the discretisation of the representative volume elements on the two-dimensional boundary value problem studied in Sect. 5.2 is briefly discussed. To this end, the evolution of the effective macroscale conductivity tensor for three different microscale discretisations is provided in Fig. 7. It is observed that the influence of the finite element discretisation on the simulation results is negligible compared to the influence of the microscale deformation for the load states and discretisations analysed.

References

1. Basinski, Z.S., Dugdale, J.S.: Electrical resistivity due to dislocations in highly purified copper. *Phys. Rev. B* **32**, 2149–2155 (1985). <https://doi.org/10.1103/PhysRevB.32.2149>
2. Berthelsen, R., Denzer, R., Oppermann, P., Menzel, A.: Computational homogenisation for thermoviscoplasticity: application to thermally sprayed coatings. *Comput. Mech.* **60**(5), 739–766 (2017). <https://doi.org/10.1007/s00466-017-1436-x>
3. Berthelsen, R., Menzel, A.: Computational homogenisation of thermo-viscoplastic composites: large strain formulation and weak micro-periodicity. *Comput. Methods Appl. Mech. Eng.* **348**, 575–603 (2019). <https://doi.org/10.1016/j.cma.2018.12.032>
4. Brown, R.A.: Electrical resistivity of dislocations in metals. *J. Phys. F Met. Phys.* **7**(7), 1283–1295 (1977). <https://doi.org/10.1088/0305-4608/7/7/026>

5. Chen, Y., Au, J., Kazlas, P., Ritenour, A., Gates, H., McCreary, M.: Flexible active-matrix electronic ink display. *Nature* **423**(6936), 136 (2003). <https://doi.org/10.1038/423136a>
6. Coenen, E.W.C., Kouznetsova, V.G., Geers, M.G.D.: Enabling microstructure-based damage and localization analyses and upscaling. *Model. Simul. Mater. Sci. Eng.* **19**(7), 074008 (2011). <https://doi.org/10.1088/0965-0393/19/7/074008>
7. Cordill, M.J., Glushko, O., Kreith, J., Marx, V.M., Kirchlechner, C.: Measuring electro-mechanical properties of thin films on polymer substrates. *Microelectron. Eng.* **137**, 96–100 (2015). <https://doi.org/10.1016/j.mee.2014.08.002>
8. Eringen, A.C.: *Mechanics of Continua*. Robert E. Krieger Publishing Co, Huntington (1980)
9. Eringen, A.C., Maugin, G.A.: *Electrodynamics of Continua I: Foundations and Solid Media*. Springer, New York (1990). <https://doi.org/10.1007/978-1-4612-3226-1>
10. Axisa, F., Schmitt, P.M., Gehin, C., Delhomme, G., McAdams, E., Dittmar, A.: Flexible technologies and smart clothing for citizen medicine, home healthcare, and disease prevention. *IEEE Trans. Inf. Technol. Biomed.* **9**(3), 325–336 (2005). <https://doi.org/10.1109/TITB.2005.854505>
11. Fangye, Y.F., Miska, N., Balzani, D.: Automated simulation of voxel-based microstructures based on enhanced finite cell approach. *Arch. Appl. Mech.* **90**, 2255–2273 (2020). <https://doi.org/10.1007/s00419-020-01719-x>
12. Feyel, F., Chaboche, J.L.: FE² multiscale approach for modelling the elastoviscoplastic behaviour of long fibre SiC/Ti composite materials. *Comput. Methods Appl. Mech. Eng.* **183**(3), 309–330 (2000). [https://doi.org/10.1016/S0045-7825\(99\)00224-8](https://doi.org/10.1016/S0045-7825(99)00224-8)
13. Geers, M., Kouznetsova, V., Brekelmans, W.: Multi-scale computational homogenization: trends and challenges. *J. Comput. Appl. Math.* **234**(7), 2175–2182 (2010). <https://doi.org/10.1016/j.cam.2009.08.077>
14. Gu, T., Castelnau, O., Forest, S., Hervé-Luanco, E., Lecouturier, F., Proudhon, H., Thilly, L.: Multiscale modeling of the elastic behavior of architected and nanostructured Cu–Nb composite wires. *Int. J. Solids Struct.* **121**, 148–162 (2017). <https://doi.org/10.1016/j.ijsolstr.2017.05.022>
15. Harrison, W.A.: Resistivity due to dislocations in copper. *J. Phys. Chem. Solids* **5**(1), 44–46 (1958). [https://doi.org/10.1016/0022-3697\(58\)90130-6](https://doi.org/10.1016/0022-3697(58)90130-6)
16. Hutter, K., Ven, A.A.F., Ursescu, A.: *Electromagnetic Field Matter Interactions in Thermoelastic Solids and Viscous Fluids*. Lecture Notes in Physics, vol. 710. Springer, Berlin (2006)
17. Jänicke, R., Steeb, H.: Minimal loading conditions for higher-order numerical homogenisation schemes. *Arch. Appl. Mech.* **82**(8), 1075–1088 (2012). <https://doi.org/10.1007/s00419-012-0614-8>
18. Javili, A., Chatzigeorgiou, G., Steinmann, P.: Computational homogenization in magneto-mechanics. *Int. J. Solids Struct.* **50**(25), 4197–4216 (2013). <https://doi.org/10.1016/j.ijsolstr.2013.08.024>
19. Kaiser, T., Menzel, A.: An electro-mechanically coupled computational multiscale formulation for electrical conductors. *Arch. Appl. Mech.* **91**, 1509–1526 (2021). <https://doi.org/10.1007/s00419-020-01837-6>
20. Keip, M.A., Steinmann, P., Schröder, J.: Two-scale computational homogenization of electro-elasticity at finite strains. *Comput. Methods Appl. Mech. Eng.* **278**, 62–79 (2014). <https://doi.org/10.1016/j.cma.2014.04.020>
21. Khalaqzaman, M., Xu, B.X., Ricker, S., Müller, R.: Computational homogenization of piezoelectric materials using FE² to determine configurational forces. *Tech. Mech.* **32**(1), 21–37 (2012)
22. Kim, S., Kwon, H.J., Lee, S., Shim, H., Chun, Y., Choi, W., Kwack, J., Han, D., Song, M., Kim, S., Mohammadi, S., Kee, I., Lee, S.Y.: Low-power flexible organic light-emitting diode display device. *Adv. Mater.* **23**(31), 3511–3516 (2011). <https://doi.org/10.1002/adma.201101066>
23. Koch, A., Bonhage, M., Teschke, M., Lücker, L., Behrens, B.A., Walther, F.: Electrical resistance-based fatigue assessment and capability prediction of extrudates from recycled field-assisted sintered EN AW-6082 aluminium chips. *Mater. Char.* **169**, 110644 (2020). <https://doi.org/10.1016/j.matchar.2020.110644>
24. Kouznetsova, V.G., Brekelmans, W.A.M., Baaijens, F.P.T.: An approach to micro–macro modeling of heterogeneous materials. *Comput. Mech.* **27**(1), 37–48 (2001). <https://doi.org/10.1007/s004660000212>
25. Kouznetsova, V.G., Geers, M.G.D., Brekelmans, W.A.M.: Multi-scale constitutive modelling of heterogeneous materials with a gradient-enhanced computational homogenization scheme. *Int. J. Numer. Methods Eng.* **54**(8), 1235–1260 (2002). <https://doi.org/10.1002/nme.541>
26. Kouznetsova, V.G., Geers, M.G.D., Brekelmans, W.A.M.: Multi-scale second-order computational homogenization of multi-phase materials: a nested finite element solution strategy. *Comput. Methods Appl. Mech. Eng.* **193**(48), 5525–5550 (2004). <https://doi.org/10.1016/j.cma.2003.12.073>
27. Miehe, C., Koch, A.: Computational micro-to-macro transitions of discretized microstructures undergoing small strains. *Arch. Appl. Mech.* **72**(4–5), 300–317 (2002). <https://doi.org/10.1007/s00419-002-0212-2>
28. Miehe, C., Schotte, J., Schröder, J.: Computational micro-macro transitions and overall moduli in the analysis of polycrystals at large strains. *Comput. Mater. Sci.* **16**(1), 372–382 (1999). [https://doi.org/10.1016/S0927-0256\(99\)00080-4](https://doi.org/10.1016/S0927-0256(99)00080-4)
29. Miehe, C., Schröder, J., Bayreuther, C.: On the homogenization analysis of composite materials based on discretized fluctuations on the micro-structure. *Acta Mech.* **155**(1–2), 1–16 (2002). <https://doi.org/10.1007/BF01170836>
30. Miehe, C., Schröder, J., Schotte, J.: Computational homogenization analysis in finite plasticity. Simulation of texture development in polycrystalline materials. *Comput. Methods Appl. Mech. Eng.* **171**(3), 387–418 (1999). [https://doi.org/10.1016/S0045-7825\(98\)00218-7](https://doi.org/10.1016/S0045-7825(98)00218-7)
31. Mitsubayashi, K., Wakabayashi, Y., Murotomi, D., Yamada, T., Kawase, T., Iwagaki, S., Karube, I.: Wearable and flexible oxygen sensor for transcutaneous oxygen monitoring. *Sens. Actuators B Chem.* **95**(1), 373–377 (2003). [https://doi.org/10.1016/S0925-4005\(03\)00441-6](https://doi.org/10.1016/S0925-4005(03)00441-6)
32. Ostoja-Starzewski, M.: Macrohomogeneity condition in dynamics of micropolar media. *Arch. Appl. Mech.* **81**(7), 899–906 (2011). <https://doi.org/10.1007/s00419-010-0456-1>
33. Özdemir, I., Brekelmans, W.A.M., Geers, M.G.D.: FE² computational homogenization for the thermo-mechanical analysis of heterogeneous solids. *Comput. Methods Appl. Mech. Eng.* **198**(3), 602–613 (2008). <https://doi.org/10.1016/j.cma.2008.09.008>
34. Santapuri, S.: Thermodynamic restrictions on linear reversible and irreversible thermo-electro-magneto-mechanical processes. *Heliyon* **2**(10), e00164 (2016). <https://doi.org/10.1016/j.heliyon.2016.e00164>

35. Schröder, J.: Derivation of the localization and homogenization conditions for electro-mechanically coupled problems. *Comput. Mater. Sci.* **46**(3), 595–599 (2009). <https://doi.org/10.1016/j.commatsci.2009.03.035>
36. Schröder, J., Balzani, D., Brands, D.: Approximation of random microstructures by periodic statistically similar representative volume elements based on lineal-path functions. *Arch. Appl. Mech.* **81**(7), 975–997 (2011). <https://doi.org/10.1007/s00419-010-0462-3>
37. Sengupta, A., Papadopoulos, P., Taylor, R.L.: A multiscale finite element method for modeling fully coupled thermomechanical problems in solids. *Int. J. Numer. Methods Eng.* **91**(13), 1386–1405 (2012). <https://doi.org/10.1002/nme.4320>
38. Spieler, C., Kästner, M., Goldmann, J., Brummund, J., Ulbricht, V.: XFEM modeling and homogenization of magnetoactive composites. *Acta Mech.* **224**(11), 2453–2469 (2013). <https://doi.org/10.1007/s00707-013-0948-5>
39. Temizer, İ., Wriggers, P.: Homogenization in finite thermoelasticity. *J. Mech. Phys. Solids* **59**(2), 344–372 (2011). <https://doi.org/10.1016/j.jmps.2010.10.004>
40. Webb, J.P.: Imposing linear constraints in finite-element analysis. *Commun. Appl. Numer. Methods* **6**(6), 471–475 (1990). <https://doi.org/10.1002/cnm.1630060607>

Publisher's Note Springer Nature remains neutral with regard to jurisdictional claims in published maps and institutional affiliations.